RSC Advances

PAPER

View Article Online
View Journal | View Issue

Cite this: *RSC Adv.*, 2020, **10**, 4664

Surface reduction properties of ceria–zirconia solid solutions: a first-principles study†

Xuesong Cao, Chenxi Zhang,* Zehua Wang, Wen Liu and Xiaomin Sun*

Received 15th November 2019
Accepted 10th January 2020

DOI: 10.1039/c9ra09550k

rsc.li/rsc-advances

Based on the density functional theory (DFT), the reduction properties of $Ce_{1-x}Zr_xO_2$ (110) surfaces were systematically calculated using CO as a probe for thermodynamic study, and a large supercell was applied to build the whole composition range (x = 0.125, 0.250, 0.375, 0.500, 0.625, 0.750, 0.875). From the calculated energy barriers of CO oxidation by lattice oxygen, we found that composition $Ce_{0.875}Zr_{0.125}O_2$ exhibited the most promising catalytic effectiveness with the lowest activation energy of 0.899 eV. Moreover, the active surface O_{3c} ions coordinated by two Zr ions and one Ce ion were facilely released from their bulk positions than the O_{3c} ions surrounded by two Ce ions and one Zr ion on $Ce_{0.625}Zr_{0.375}O_2$, $Ce_{0.500}Zr_{0.500}O_2$, and $Ce_{0.375}Zr_{0.625}O_2$ (110) surfaces. This difference could be explained by the binding strength of O_{3c} with different neighboring cations.

1. Introduction

Ceria–zirconia ($Ce_{1-x}Zr_xO_2$) solid solutions exhibit superior performance as heterogeneous catalytic materials due to its good thermal stability,[1,2] excellent oxygen storage/release capacity and reducibility.[3–5] In the last few decades, $Ce_{1-x}Zr_xO_2$ has been extensively used as an active component in three-way catalysts (TWCs) to expand the air-to-fuel ratio operating window, ensuring the effective elimination of carbon monoxide (CO), nitrogen oxides (NO_x), and hydrocarbons (HCs) during engine operation.[6] Besides, water gas shift reaction,[7] NH_3 selective catalytic reduction,[8] catalytic oxidation of volatile organic compounds (VOCs)[9] and various catalytic reactions also can be promoted by $Ce_{1-x}Zr_xO_2$.

$Ce_{1-x}Zr_xO_2$ solid solutions with different compositions result in different catalytic performance and surface properties. Great efforts have been made to investigate the most promising $Ce_{1-x}Zr_xO_2$ compositions for OSC,[10–13] which is closely related to the reduction behavior. Madier *et al.*[10] observed that $Ce_{0.63}Zr_{0.37}O_2$ had the maximum CO uptake across the whole composition range, with a dynamic OSC of 219 μmol O per g at 400 °C. Boaro *et al.*[11] proposed that $Ce_{1-x}Zr_xO_2$ with $0.2 < x < 0.5$ showed an increased CO oxidation activity under cycling feed-stream conditions. For heterogeneous catalytic reactions, the most important is the surface redox properties.[14] To obtain the optimum composition (Ce/Zr ratio), evaluation of the surface reducibility of $Ce_{1-x}Zr_xO_2$, especially the Ce^{4+}/Ce^{3+} redox behavior is necessary.

Oxygen vacancy formation energies at surfaces have been calculated using the DFT + U (U = 5.0 eV) method, by comparing the formation energies of CeO_2 (110) surface (2.30 eV) and $Ce_{0.75}Zr_{0.25}O_2$ (110) surface (0.94 eV);[15] Zr-doping (25% in this work) dramatically improved the reduction properties of ceria. In contrast, Zr-doping in CeO_2 (111) surface and ceria bulk only lowered the formation energies by 0.52 eV (ref. 16) and 0.62 eV,[17] respectively. To explain the lowering of the surface reduction energy, the electronic structure was obtained *via* the density of states (DOS) and partial charge density distribution. Yang *et al.*[15] found that for the $Ce_{0.75}Zr_{0.25}O_{2-x}$ (110) slab, the excess electrons localized on a surface of Ce-ion and on a subsurface of Ce-ion were stabilized by the crystal potential and occupied the gap states lower in energy compared to the CeO_{2-x} (110) surface. Balducci *et al.*[18] suggested that the smaller Zr dopants removed the strain caused by the increase in the ionic size when Ce^{4+} changed to Ce^{3+}, which is responsible for the improvement in the reducibility.

In the present work, we explored the CO oxidation mechanisms and energetics on $Ce_{1-x}Zr_xO_2$ (110) surfaces, using periodic DFT computation. The catalytic models were built from a 2 × 2 × 2 supercell to cover the whole composition range (x = 0.125, 0.250, 0.375, 0.500, 0.625, 0.750, 0.875). The main focus of this paper is to determine how the Ce/Zr ratio affects the surface reducibility of $Ce_{1-x}Zr_xO_2$, which has not been systematically calculated. Furthermore, low-temperature oxidation of CO is of practical importance for pollution control in many industrial processes, such as lowering automotive emissions.[19,20] Our investigation provides an atomic-scale insight for the design of efficient and economical heterogeneous catalysts.

Environment Research Institute, Shandong University, Qingdao 266200, P. R. China. E-mail: caoxueshine@163.com; sdzhangcx@163.com; zhstart13@foxmail.com; lwen951014@163.com; sxmwch@sdu.edu.cn

† Electronic supplementary information (ESI) available. See DOI: 10.1039/c9ra09550k

2. Computational details

2.1. Computational methods

In this study, all geometric optimization and calculations were performed by using the DMol^3 software package in Material Studio,[21,22] based on the periodic DFT method. The generalized gradient approximation (GGA) with Perdew–Burke–Ernzerhof (PBE)[23] was implemented as the exchange–correlation functional. The double numerical plus d-function (DND) basis set was used to optimize all spin unrestricted structures. The Ce ($4f^1$, $5s^2$, $5p^6$, $5d^1$, $6s^2$) and Zr ($4s^2$, $4p^6$, $4d^2$, $5s^2$) electrons were treated as valence electrons using the effective core potential (ECP) method.[24] The electrons of O, C and N atoms were treated using the all electron method. Specifically, a Fermi smearing of 0.005 Ha and an orbital cutoff of 5.0 Å were used to improve the computational performance. A grid of $1 \times 1 \times 1$ Monkhorst–Pack *k*-points was applied to perform integration in the first Brillouin zone.[25] The SCF tolerance was employed to 1.0×10^{-5} Ha, and then the convergence criteria of maximum energy change, maximum force, and maximum displacement were set as 2.0×10^{-5} Ha, 0.004 Ha Å^{-1}, and 0.005 Å, respectively.

The adsorption energy (E_{ads}) of the adsorbate was defined as follows:

$$E_{ads} = E_{(substrate+adsorbate)} - E_{(substrate)} - E_{(adsorbate)} \quad (1)$$

where $E_{(substrate+adsorbate)}$, $E_{(substrate)}$ and $E_{(adsorbate)}$ represent the total energies of the substrate–adsorbate system, the substrate and adsorbate, respectively. The more negative E_{ads}, the more strongly the adsorbate binds with the substrate. Linear synchronous transit and quadratic synchronous transit (LST/QST) method[26,27] was applied to isolate the transition states (TS) and calculated the corresponding activation barriers (E_a). The transition state configurations were identified by the vibrational analysis to confirm a single imaginary frequency corresponding to the reaction mode. The reaction energy (ΔE) and activation barrier energy (E_a) were defined as follows:

$$\Delta E = E_{FS} - E_{IS} \quad (2)$$

$$E_a = E_{TS} - E_{IS} \quad (3)$$

where E_{IS}, E_{TS} and E_{FS} represent the total energies of initial state (IS), transition state (TS), and final state (FS), respectively.

2.2. Computational models

Ceria is a cubic fluorite structure with a space group $Fm\bar{3}m$; the optimized lattice parameter was 5.478 Å, which is in good agreement with the experimental result of 5.411 Å.[28] Moreover, cubic zirconia (c-ZrO_2, the $Fm\bar{3}m$ space group) is also attributed to fluorite oxides. CeO_2 and c-ZrO_2 are interesting as the limiting forms of ceria–zirconia. Our calculated lattice constant for c-ZrO_2 was 5.112 Å, the corresponding experimental value was 5.090 Å.[29]

The computational model in this study was a $2 \times 2 \times 2$ supercell with 96-atom built from a conventional 12-atom unit cell of bulk CeO_2. To be consistent with the models studied by Wang *et al.*,[12,30] the lattice substituting model was used to model $Ce_{1-x}Zr_xO_2$. In the supercell, 4, 8, 12, 16, 20, 24 and 28 Zr-doping atoms were introduced to replace Ce atoms to represent stoichiometric $Ce_{0.875}Zr_{0.125}O_2$, $Ce_{0.750}Zr_{0.250}O_2$, $Ce_{0.625}Zr_{0.375}O_2$, $Ce_{0.500}Zr_{0.500}O_2$, $Ce_{0.375}Zr_{0.625}O_2$, $Ce_{0.250}Zr_{0.750}O_2$, and $Ce_{0.125}Zr_{0.875}O_2$ bulk (see Fig. 1), respectively. Besides, $Ce_{1-x}Zr_xO_2$ (110) surfaces were cleaved due to its lower surface energy and Ce^{4+}/Ce^{3+} reduction energy.[31] A 15 Å vacuum thickness was applied to eliminate slab–slab interactions. The $Ce_{1-x}Zr_xO_2$ (110) slabs consist of four atomic layers with the bottom two layers kept fixed in their bulk positions and the others were relaxed.

The DFT calculation with a Hubbard U correction (DFT + U) was applied to describe the electronic properties of CeO_2 and ZrO_2, where $U = 5$ eV was suggested to be proper for modeling on stoichiometric and reduced CeO_2 and ZrO_2 surfaces.[15,32] However, previous researches indicated that plain DFT calculations could provide a reasonable prediction of reduction energies, even better than that from DFT + U.[33,34] To ascertain the importance of the U parameter, we have calculated the oxygen vacancy formation energies on $Ce_{0.875}Zr_{0.125}O_2$ (110) surface with $U = 5$ eV (0.472 eV) and without incorporating U (0.476 eV). The vacancy formation energy without incorporating U was within 1% of $U = 5$ eV ones. Hence, the DFT + U method was not considered in the current work.

3. Results

3.1. CO oxidation on $Ce_{0.875}Zr_{0.125}O_2$ (110) surface

Conserving $Ce_{0.875}Zr_{0.125}O_2$ (110) surface stoichiometry with bulk, top surface layer and the subsurface layer of the slab contained sixteen Ce^{4+}, two of the top surface layer Ce^{4+} were replaced with Zr^{4+}. To better understand the catalytic mechanism, the adsorption behaviors of CO gas molecules on $Ce_{0.875}Zr_{0.125}O_2$ (110) surface were carefully discussed. We identified nine adsorption sites (Fig. S1(a)†): (1) the top site of Zr (Zr_T); (2) the top site of Ce (Ce_T); (3) the top site of O (O_{T1}, O_{T2}); (4) the 4-fold O-hollow site (O_{H1}, O_{H2}); (5) the bridge site between two O atoms (O_{b1}, O_{b2}, O_{b3}). All the optimized configurations were illustrated in Fig. S1† and the calculated adsorption energies of CO on $Ce_{0.875}Zr_{0.125}O_2$ (110) surface were summarized in Table S1.† We found that the adsorption of CO on the top site of Zr (Fig. S1(b)†) was the most stable configuration with an adsorption energy of −0.569 eV. Moreover, Zr-doping could increase the binding energy of CO with an interface, by comparing the calculated binding energy of Zr-doped ceria (≈ −0.4 eV) and ceria (≈ −0.2 eV).[34,35]

It is widely believed[36,37] that the detailed mechanism of CO oxidation on CeO_2 surface through the Mars–van Krevelen (MvK) mechanism,[38] in which CO extracts a surface lattice oxygen to form CO_2 and leaves behind an oxygen vacancy (O_V), and then gas phase O_2 replenishes the oxygen vacancy site to complete the catalytic cycle. For the reaction mechanism of a single CO interacting with one lattice O of $Ce_{0.875}Zr_{0.125}O_2$ (110) surface, the calculated energy profile and structure models of the reactant, transition state and product were presented in Fig. 2.

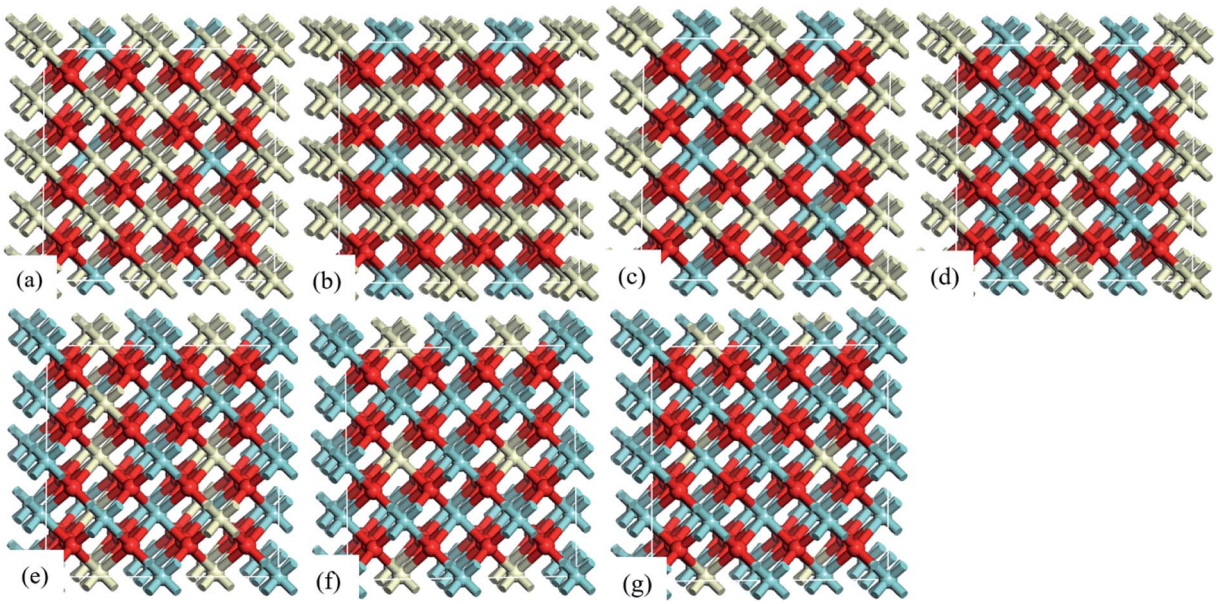

Fig. 1 The 96-atom 2 × 2 × 2 supercell models of stoichiometric (a) $Ce_{0.875}Zr_{0.125}O_2$, (b) $Ce_{0.750}Zr_{0.250}O_2$, (c) $Ce_{0.625}Zr_{0.375}O_2$, (d) $Ce_{0.500}Zr_{0.500}O_2$, (e) $Ce_{0.375}Zr_{0.625}O_2$, (f) $Ce_{0.250}Zr_{0.750}O_2$ and (g) $Ce_{0.125}Zr_{0.875}O_2$. Red, ivory and cyan spheres represent the O, Ce and Zr atoms, respectively.

We took the state with CO gas molecule adsorbed at Zr_T site ($E_{ads} = -0.569$ eV) as the initial state (IS), the distance between C atom and surface lattice O was 2.559 Å. Subsequently, the CO molecule directly incorporated a surface O from the gas phase following the so-called Eley–Rideal (ER) mechanism. The energy barrier for this process was 0.899 eV, this result was a little lower than that of CO oxidation on the Pd_1/CeO_2 (110) surface (0.954 eV),[39] indicating that the catalytic activity of ceria–zirconia solid solutions was comparable with traditional ceria-based single-atom catalyst. In the final state (FS), gas phase CO_2 formed above the $Ce_{0.875}Zr_{0.125}O_2$ (110) surface containing an oxygen vacancy, meanwhile, the surface oxygen anion neighboring the vacancy moved toward the Ce–Zr bridge site by about 1.281 Å.

3.2. CO oxidation on $Ce_{0.750}Zr_{0.250}O_2$ (110) surface

On the $Ce_{0.750}Zr_{0.250}O_2$ (110) surface, four of the top surface layer Ce atoms were replaced with Zr ($Ce_{0.750}Zr_{0.250}O_2$, see Fig. 3). Based on the adsorption behaviors of CO on $Ce_{0.875}Zr_{0.125}O_2$ (110) surface as discussed above, we also considered CO adsorbtion at the Zr_T site as the initial state for CO oxidation on $Ce_{1-x}Zr_xO_2$ (x = 0.250, 0.375, 0.500, 0.625, 0.750, 0.875) (110) surfaces. As shown in Fig. 3 (IS), CO combined with a Zr atom, the distance was determined to be 2.562 Å and the binding energy was −0.600 eV. In the transition state (TS, Fig. 3), adsorbed CO molecule migrated to a lattice O and the distance decreased to 2.103 Å. This process needed to overcome an activation barrier of 1.555 eV and was exothermic by 2.367 eV. With the formation of CO_2 (FS, Fig. 3), the neighboring lattice O moved to the Ce–Zr bridge site, the bond of Ce–O, and Zr–O were 2.485 Å and 2.048 Å, respectively.

3.3. CO oxidation on $Ce_{0.625}Zr_{0.375}O_2$ and $Ce_{0.500}Zr_{0.500}O_2$ (110) surfaces

On the $Ce_{0.625}Zr_{0.375}O_2$ (110) surface, four of the top surface layer Ce atoms and two of the subsurface layer Ce atoms were replaced with Zr ($Ce_{0.625}Zr_{0.375}O_2$, see Fig. 4). In this case, four surface lattice oxygen neighboring Zr_T sites were not all equivalent: three of these oxygen (O_A) bonded with two Ce^{4+} and one Zr^{4+}, while one of the oxygen (O_B) bonded with two Zr^{4+} and one Ce^{4+}. There are two pathways for CO oxidation with different surface lattice oxygen; the corresponding energy profile and structure models are illustrated in Fig. 4. From the initial state (IS), CO adsorbed at the Zr_T site of $Ce_{0.625}Zr_{0.375}O_2$ (110) surface, the adsorption energy was calculated to be −0.607 eV. Then, CO

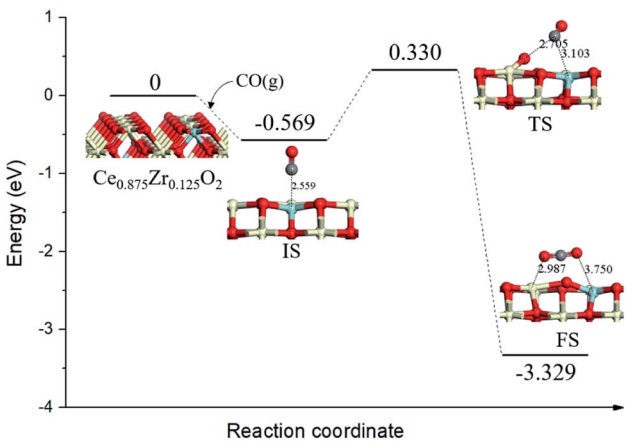

Fig. 2 Calculated energy profile and structures of key states of CO oxidation by lattice oxygen on $Ce_{0.875}Zr_{0.125}O_2$ (110) surface. Gray spheres represent the C atoms.

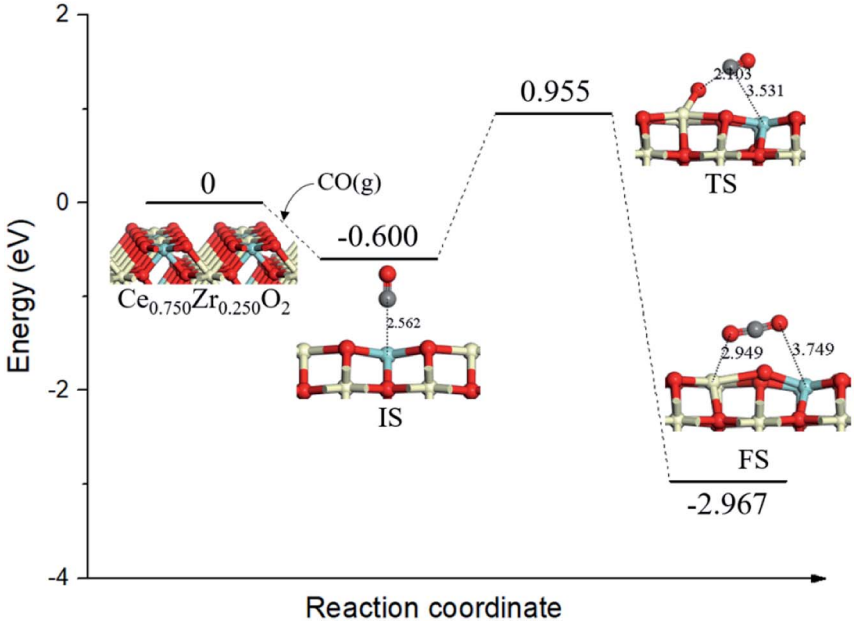

Fig. 3 Calculated energy profile and structures of key states of CO oxidation by lattice oxygen on $Ce_{0.750}Zr_{0.250}O_2$ (110) surface.

extracted O_A *via* TS1; this process needed a higher energy barrier of 2.239 eV and the reaction energy was −2.216 eV. Alternatively, CO might combine with O_B, going through another transition state (TS2) with a smaller energy barrier of 1.175 eV.

On the $Ce_{0.500}Zr_{0.500}O_2$ (110) surface, four of the top surface layer Ce atoms and four of the subsurface layer Ce atoms were replaced with Zr ($Ce_{0.500}Zr_{0.500}O_2$, see Fig. S2†). According to our calculations, the detailed mechanisms of CO oxidation on the $Ce_{0.500}Zr_{0.500}O_2$ (110) surface were similar to that on the $Ce_{0.625}Zr_{0.375}O_2$ (110) surface, as shown in Fig. S2.†

3.4. CO oxidation on $Ce_{0.375}Zr_{0.625}O_2$, $Ce_{0.250}Zr_{0.750}O_2$ and $Ce_{0.125}Zr_{0.875}O_2$ (110) surfaces

On the $Ce_{0.375}Zr_{0.625}O_2$ (110) surface, four of the top surface layer Ce atoms and six of the subsurface layer Ce atoms were replaced with Zr ($Ce_{0.375}Zr_{0.625}O_2$, see Fig. 5). Two possible

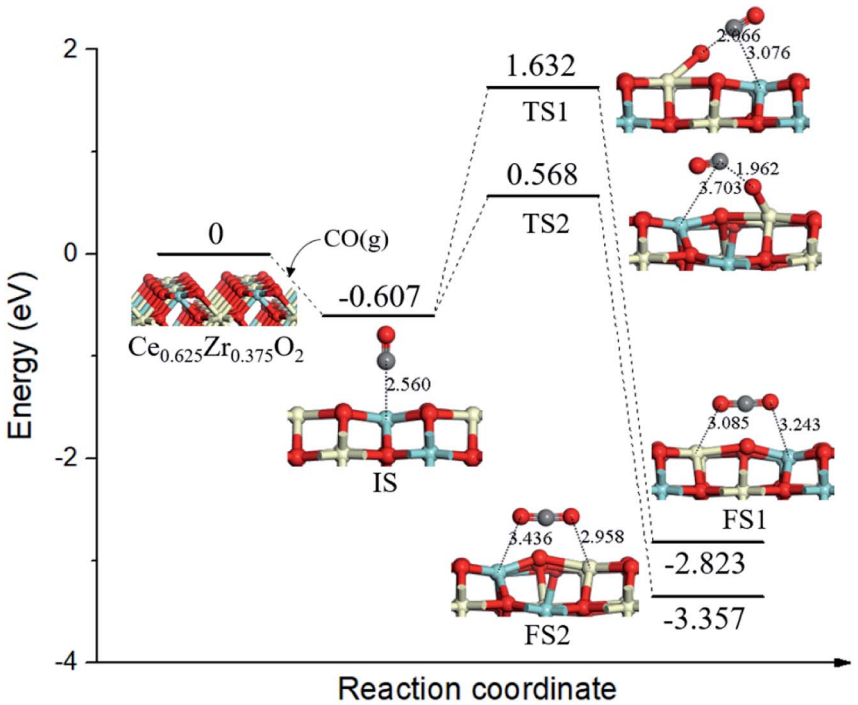

Fig. 4 Calculated energy profile and structures of key states of CO oxidation by lattice oxygen on $Ce_{0.625}Zr_{0.375}O_2$ (110) surface.

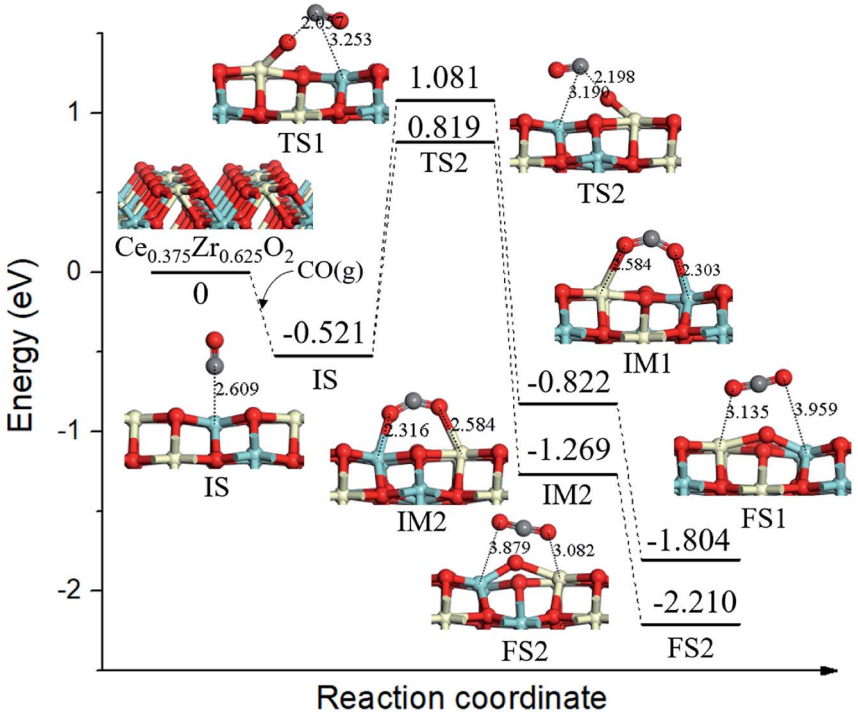

Fig. 5 Calculated energy profile and structures of key states of CO oxidation by lattice oxygen on $Ce_{0.375}Zr_{0.625}O_2$ (110) surface.

reaction routes were estimated based on the two types of surface lattice oxygens (O_A and O_B) as mentioned above. For the first route, the migration of adsorbed CO species (−0.521 eV, IS, Fig. 5) toward O_A led to the formation of a bent CO_2 species (IM1, Fig. 5) *via* TS1 ($E_a = 1.602$ eV, Fig. 5); IM1 was calculated to be 0.301 eV, more stable than the IS. Then IM1 evolved to the final state (FS1, Fig. 5) through an almost barrierless process. The second route was determined to be the same as that of the first route.

On the $Ce_{0.250}Zr_{0.750}O_2$ (110) surface, four of the top surface layer Ce atoms and eight of the subsurface layer Ce atoms were replaced with Zr ($Ce_{0.250}Zr_{0.750}O_2$, see Fig. S3†). On the

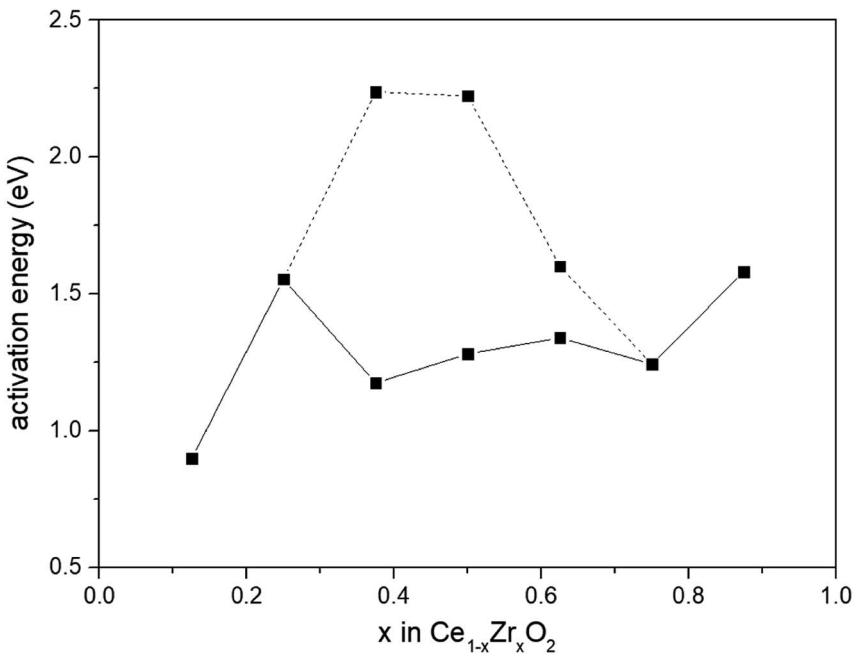

Fig. 6 Activation energies for CO oxidation by lattice oxygen on $Ce_{1-x}Zr_xO_2$ ($x = 0.125, 0.250, 0.375, 0.500, 0.625, 0.750, 0.875$) (110) surfaces.

$Ce_{0.125}Zr_{0.875}O_2$ (110) surface, six of the top surface layer Ce atoms and eight of the subsurface layer Ce atoms were replaced with Zr ($Ce_{0.125}Zr_{0.875}O_2$, see Fig. S4†). Calculated energy profile and structure models were presented in Fig. S3 and S4† for CO oxidation on $Ce_{0.250}Zr_{0.750}O_2$ and $Ce_{0.125}Zr_{0.875}O_2$ (110) surfaces, respectively.

4. Discussion

In this work, the adsorption energies and barrier energies of CO oxidation on various $Ce_{1-x}Zr_xO_2$ (110) surfaces were systematically studied using the DFT method. These calculation results provide some insights into the surface reducibility of $Ce_{1-x}Zr_xO_2$ toward CO oxidation. From the adsorption behaviors of CO on the $Ce_{0.875}Zr_{0.125}O_2$ (110) surface, we found that Zr_T was the most favorable active site owing to the maximum adsorption energy. Besides, according to the adsorption energies of CO on the CeO_2 (110) surface ($E_{ads} \approx -0.2$ eV)[34,35] and ZrO_2 (110) surface ($E_{ads} \approx -0.6$ eV),[40] it also could be concluded that CO preferred to interact with Zr atoms and adsorb on the top site of Zr on $Ce_{1-x}Zr_xO_2$ (110) surfaces. However, it is noteworthy that CO adsorption on $Ce_{1-x}Zr_xO_2$ (110) surfaces were still rather weak ($E_{ads} \approx -0.6$ eV), indicating that the feasible CO oxidation mechanism was gas-phase CO molecule directly extracting

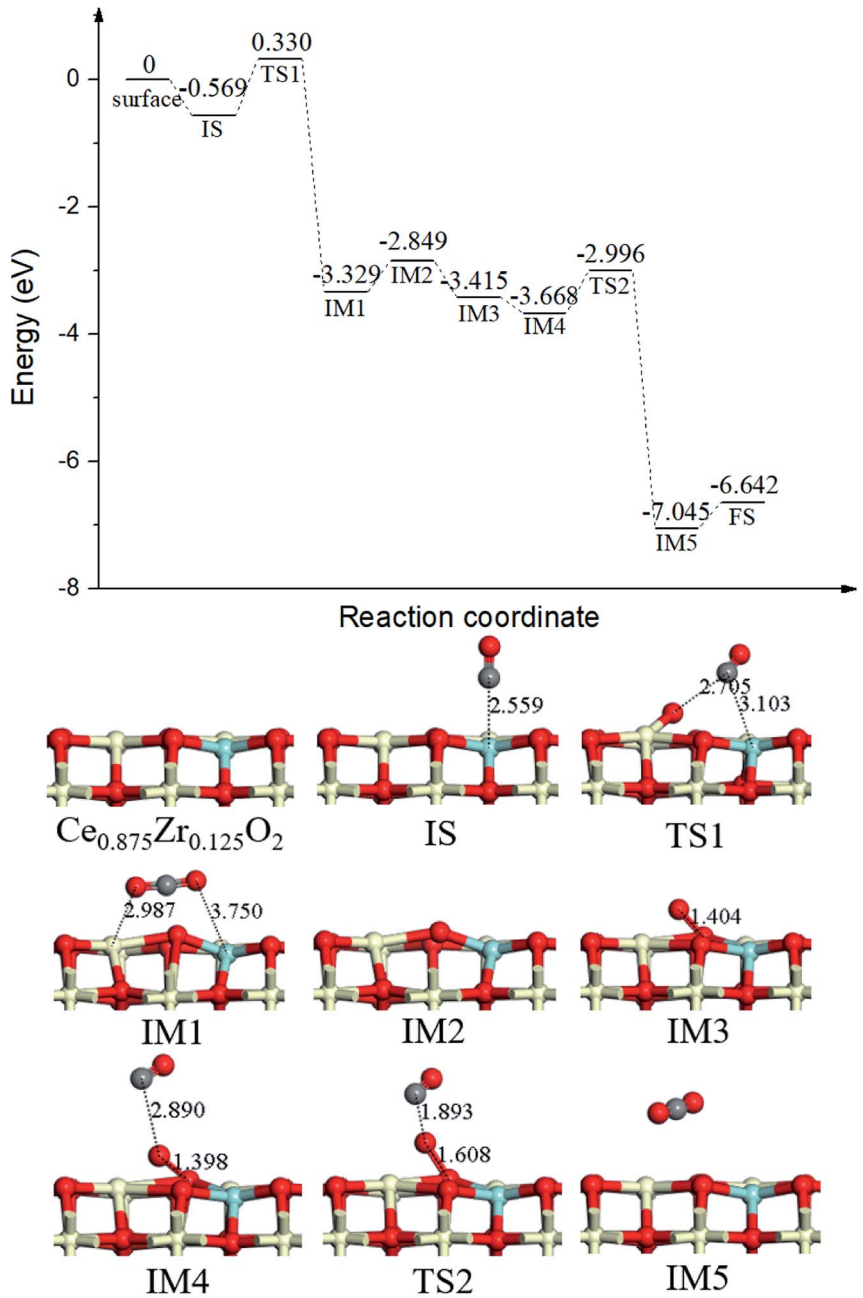

Fig. 7 Calculated energy profile and structures of key states for the catalytic cycle of CO oxidation on $Ce_{0.875}Zr_{0.125}O_2$ (110) surface.

surface lattice oxygen following the so-called Eley–Rideal (ER) mechanism,[36,37] exactly as CO oxidation on the CeO_2 (110) and (111) surfaces.[35]

As shown in Fig. 4, S2,† and 5, $Ce_{0.625}Zr_{0.375}O_2$, $Ce_{0.500}Zr_{0.500}O_2$, and $Ce_{0.375}Zr_{0.625}O_2$ (110) surfaces contained two types of lattice oxygens, the CO oxidation activity of these oxygens were quite different. In particular, the activation barriers of CO reacted with O_{3c} ions coordinated by two Zr ions and one Ce ion were relatively lower than O_{3c} ions surrounded by two Ce ions and one Zr ion. In the previous work, different types of surface O ions were also found on the $Ce_{0.75}Zr_{0.25}O_2$ (111) surface, and the vacancy formation energy for the surface O_{3c} surrounded by three Ce neighbors was higher than the surface O_{3c} coordinated by two Ce ions and one Zr ion.[16] We interpreted that the binding strength of O_{3c} with neighboring cations caused the difference of O_{3c} reactivity. Considering that the size of Ce ion would increase when Ce^{4+} changed to Ce^{3+}, O_{3c} ions coordinated by smaller Zr ion might promote the reduction process.[18]

We presented the activation barrier energies of CO oxidation on various $Ce_{1-x}Zr_xO_2$ (110) surfaces in Fig. 6. As we all know, the occurrence of redox reaction through a low energy barrier process was thermodynamically favorable. Therefore, energy barriers of 1.175 eV, 1.281 eV and 1.340 eV for CO oxidation on $Ce_{0.625}Zr_{0.375}O_2$, $Ce_{0.500}Zr_{0.500}O_2$ and $Ce_{0.375}Zr_{0.625}O_2$ (110) surfaces were used to compare with others. Among all the compositions, the $Ce_{0.875}Zr_{0.125}O_2$ (110) surface exhibited the most remarkable catalytic effectiveness, with the lowest energy barrier of 0.899 eV. This result was consistent with the experimental value reported by Piumetti *et al.*[41] that the $Ce_{0.9}Zr_{0.1}O_2$ catalyst shown the highest CO oxidation activity (Zr-content was in the range of 10–30%). Trovarelli *et al.*[3] observed that dynamic OSC of $Ce_{1-x}Zr_xO_2$ showed a monotonic increase with increasing Ce-content and the optimum composition was $Ce_{0.9}Zr_{0.1}O_2$. However, these results were at odds with we mentioned above, composition of $Ce_{1-x}Zr_xO_2$ with $0.2 < x < 0.5$ possessed an increased catalytic activity.[10,11,42,43] There is still an intense scientific debate on the optimum Ce/Zr composition for catalytic materials.

Finally, we completed the overall catalytic cycle of CO oxidation on the optimum $Ce_{0.875}Zr_{0.125}O_2$ (110) surface, which focused on the explanation of the gas-phase O_2 diffusion through the catalyst instead of oxygen-ion diffusion within the lattice. As shown in Fig. 7, following the first gas-phase CO_2 and one O_V formation (IM1, Fig. 7) *via* TS1 (Fig. 7, the same as in Fig. 2), the CO_2 desorbed from the surface (IM2, Fig. 7) overcoming 0.480 eV energy. Subsequently, O_2 adsorbed on the O_V site (IM3, Fig. 7), and then, the second CO molecule bound with the adsorbed O_2 to form a coadsorption configuration IM4 (Fig. 7), with the binding energy of −0.819 eV, followed by CO approaching the upper O of the adsorbed O_2 to form the second CO_2 molecule (IM5, Fig. 7) *via* TS2 (Fig. 7). The energy barrier for the second CO_2 formation was 0.672 eV, dramatically lower than that of the first CO_2 formation (0.899 eV). It is obvious that CO oxidation by surface oxygen was the elementary step in the overall catalytic cycle.

5. Conclusions

In the current work, DFT method was performed to investigate the reduction properties of $Ce_{1-x}Zr_xO_2$ ($x = 0.125$, 0.250, 0.375, 0.500, 0.625, 0.750, 0.875) (110) surfaces, using CO as a probe for the thermodynamic study. For the details of the reaction mechanism, CO preferred to adsorb on the Zr_T site with rather weak binding energies (≈ -0.6 eV), thus gas-phase CO directly extracted surface lattice O to form CO_2 and surface O_V following the Eley–Rideal (ER) mechanism. From the calculated energy barriers, we proposed that $Ce_{0.875}Zr_{0.125}O_2$ was the optimum composition to efficiently release surface lattice O. In addition, the occurrence of surface O_V had significant effects on catalytic processes.[44,45] Especially, two different types of active O_{3c} (O_A and O_B) existed on $Ce_{0.625}Zr_{0.375}O_2$, $Ce_{0.500}Zr_{0.500}O_2$ and $Ce_{0.375}Zr_{0.625}O_2$ (110) surface, the CO oxidation activity of O_B was significantly higher than that of O_A with the energy barriers of 1.175 < 2.239 eV, 1.281 < 2.224 eV and 1.340 < 1.602 eV on $Ce_{0.625}Zr_{0.375}O_2$, $Ce_{0.500}Zr_{0.500}O_2$ and $Ce_{0.375}Zr_{0.625}O_2$ (110) surface, respectively. We explained that the binding strength of active O_{3c} with neighboring cations causes the difference, and since the ionic size increased when Ce^{4+} changed to Ce^{3+} and O_{3c} ions coordinated by smaller Zr ions may facilitate the reduction process.

Conflicts of interest

There are no conflicts to declare.

Acknowledgements

This work is supported by National Natural Science Foundation of China (21607011, 21976109), Key Research and Development Project of Shandong Province (2019GSF109021, 2019GSF109037), Natural Science Foundation of Shandong Province (ZR2018MB043), the Fundamental Research Funds of Shandong University (2018JC027).

References

1 C. Bozo, F. Gaillard and N. Guilhaume, *Appl. Catal., A*, 2001, **220**, 69–77.
2 R. Zhou, X. Zhang, J. Lu, G. Hu and M. Luo, *Chem. Res. Chin. Univ.*, 2015, **31**, 288–293.
3 A. Trovarelli, F. Zamar, J. Llorca, C. d. Leitenburg, G. Dolcetti and J. T. Kiss, *J. Catal.*, 1997, **169**, 490–502.
4 M. Sugiura, *Catal. Surv. Asia*, 2003, **7**, 77–87.
5 J. Deng, S. Yuan, L. Xiong, S. Li, J. Wang and Y. Chen, *Mater. Charact.*, 2019, **155**, 109808.
6 Z. Zhang, Y. Fan, Y. Xin, Q. Li, R. Li, J. A. Anderson and Z. Zhang, *Environ. Sci. Technol.*, 2015, **49**, 7989–7995.
7 A. Łamacz, K. Matus, B. Liszka, J. Silvestre-Albero, M. Lafjah, T. Dintzer and I. Janowska, *Catal. Today*, 2018, **301**, 172–182.
8 J. Liu, X. Shi, Y. Shan, Z. Yan, W. Shan, Y. Yu and H. He, *Environ. Sci. Technol.*, 2018, **52**, 11769–11777.
9 P. M. Shah, A. N. Day, T. E. Davies, D. J. Morgan and S. H. Taylor, *Appl. Catal., B*, 2019, **253**, 331–340.

10 Y. Madier, C. Descorme, A. M. Le Govic and D. Duprez, *J. Phys. Chem. B*, 1999, **103**, 10999–11006.
11 M. Boaro, C. de Leitenburg, G. Dolcetti and A. Trovarelli, *J. Catal.*, 2000, **193**, 338–347.
12 H. Wang, X. Gong, Y. Guo, Y. Guo, G. Z. Lu and P. Hu, *J. Phys. Chem. C*, 2009, **113**, 10229–10232.
13 B. Guo, *J. Alloys Compd.*, 2019, **785**, 1121–1125.
14 C. E. Hori, H. Permana, K. Y. S. Ng, A. Brenner, K. More, K. M. Rahmoeller and D. Belton, *Appl. Catal., B*, 1998, **16**, 105–117.
15 Z. Yang, Z. Fu, Y. Wei and K. Hermansson, *Chem. Phys. Lett.*, 2008, **450**, 286–291.
16 Z. Yang, Y. Wei, Z. Fu, Z. Lu and K. Hermansson, *Surf. Sci.*, 2008, **602**, 1199–1206.
17 Z. Yang, T. K. Woo and K. Hermansson, *J. Chem. Phys.*, 2006, **124**, 224704.
18 G. Balducci, J. Kašpar, P. Fornasiero, M. Graziani, M. S. Islam and J. D. Gale, *J. Phys. Chem. B*, 1997, **101**, 1750–1753.
19 X. Xie, Y. Li, Z.-Q. Liu, M. Haruta and W. Shen, *Nature*, 2009, **458**, 746–749.
20 D. Gerçeker and I. Önal, *Appl. Surf. Sci.*, 2013, **285**, 927–936.
21 B. Delley, *J. Chem. Phys.*, 1990, **92**, 508–517.
22 B. Delley, *J. Chem. Phys.*, 2000, **113**, 7756–7764.
23 J. P. Perdew, K. Burke and M. Ernzerhof, *Phys. Rev. Lett.*, 1996, **77**, 3865–3868.
24 A. Bergner, M. Dolg, W. Küchle, H. Stoll and H. Preuß, *Mol. Phys.*, 1993, **80**, 1431–1441.
25 H. J. Monkhorst and J. D. Pack, *Phys. Rev. B: Solid State*, 1976, **13**, 5188–5192.
26 T. A. Halgren and W. N. Lipscomb, *Chem. Phys. Lett.*, 1977, **49**, 225–232.
27 R. Elber and M. Karplus, *Chem. Phys. Lett.*, 1987, **139**, 375–380.
28 K. A. Gschneider, L. Eyring and T. A. Roth, *J. Electrochem. Soc.*, 1979, **126**, 464C.
29 C. J. Howard, R. J. Hill and B. E. Reichert, *Acta Crystallogr., Sect. B: Struct. Sci.*, 1988, **44**, 116–120.
30 H. Wang, Y. Guo, G. Lu and P. Hu, *Angew. Chem., Int. Ed.*, 2009, **48**, 8289–8292.
31 G. Balducci, J. Kašpar, P. Fornasiero, M. Graziani and M. S. Islam, *J. Phys. Chem. B*, 1998, **102**, 557–561.
32 S. Fabris, S. de Gironcoli, S. Baroni, G. Vicario and G. Balducci, *Phys. Rev. B: Condens. Matter Mater. Phys.*, 2005, **71**, 041102.
33 M. Fronzi, S. Piccinin, B. Delley, E. Traversa and C. Stampfl, *Phys. Chem. Chem. Phys.*, 2009, **11**, 9188–9199.
34 M. Huang and S. Fabris, *J. Phys. Chem. C*, 2008, **112**, 8643–8648.
35 F. Chen, D. Liu, J. Zhang, P. Hu, X.-Q. Gong and G. Lu, *Phys. Chem. Chem. Phys.*, 2012, **14**, 16573–16580.
36 Z. Wu, M. Li and S. H. Overbury, *J. Catal.*, 2012, **285**, 61–73.
37 M. Boaro, F. Giordano, S. Recchia, V. D. Santo, M. Giona and A. Trovarelli, *Appl. Catal., B*, 2004, **52**, 225–237.
38 P. Mars and D. W. van Krevelen, *Chem. Eng. Sci.*, 1954, **3**, 41–59.
39 W. Song, Y. Su and E. J. M. Hensen, *J. Phys. Chem. C*, 2015, **119**, 27505–27511.
40 X. Cao, C. Zhang, Z. Wang and X. Sun, *Int. J. Mol. Sci.*, 2019, **20**, 6129.
41 M. Piumetti, S. Bensaid, D. Fino and N. Russo, *Appl. Catal., B*, 2016, **197**, 35–46.
42 J. Kašpar, P. Fornasiero and M. Graziani, *Catal. Today*, 1999, **50**, 285–298.
43 J.-P. Cuif, G. Blanchard, O. Touret, M. Marczi and E. Quéméré, 1996.
44 Y. Song, L. Yin, J. Zhang, P. Hu, X. Gong and G. Lu, *Surf. Sci.*, 2013, **618**, 140–147.
45 H. Gao, *Appl. Catal., A*, 2017, **529**, 156–166.